

Liquid transfer from single cavities to rotating rolls

Diego M. Campana^{1,2} and Marcio S. Carvalho^{2,†}

¹Instituto de Desarrollo Tecnológico para la Industria Química (INTEC-CONICET), Güemes 3450, Santa Fe (3000), República Argentina

²Department of Mechanical Engineering, Pontifícia Universidade Católica do Rio de Janeiro (PUC-RIO), Rio de Janeiro, RJ 22453-900, Brazil

(Received 17 May 2013; revised 19 March 2014; accepted 29 March 2014;
first published online 23 April 2014)

In this work we study computationally the dynamics of a liquid bridge formed between a two-dimensional trapezoidal cavity, which represents an axisymmetric cell or a plane groove engraved in a roll, and a moving plate. The flow is a model of the liquid transfer process in gravure printing systems. The considered plate kinematics represents the actual motion of a roll-to-roll system, which includes extension, shear and rotation relative to the cavity. The fluid flow is modelled by solving the Stokes equations, discretized with the finite element method; the evolving free surfaces are accommodated by employing a pseudosolid mesh deforming algorithm. The results show that as the roll radius is reduced, thus increasing the lateral and rotational motions of the top plate relative to the cavity, a larger volume of liquid is transferred to the plate. However, due to lateral displacement of the contact lines, special care must be taken concerning the wettability properties of the substrate to avoid errors in the pattern fidelity. The predictions also show a strong nonlinear behaviour of the liquid fraction extracted from a cavity as a function of the capillary number. At high capillary numbers the fluid dynamics is mainly controlled by the extensional motion due to the strong contact line pinning. However, at low values of the capillary number, the contact lines have higher mobility and the liquid fraction primarily depends on the lateral and rotational plate velocity. These mechanisms tend to drag the fluid outside the cavity and increase the liquid fraction transferred to the plate, as has been observed in experiments.

Key words: contact lines, gravure printing, liquid bridges

1. Introduction

In recent years, printing technology has gained much attention because of its potential applicability in the production of flexible electronics devices. One important example is the production of polymer solar cells, which are a promising solution for cost reduction of photovoltaic technologies (Krebs 2009). Polymer solar cells are suitable for manufacture by using high-scale film-forming techniques like slot and gravure coating and also by printing technologies like screen, pad or gravure

† Email address for correspondence: masc@puc-rio.br

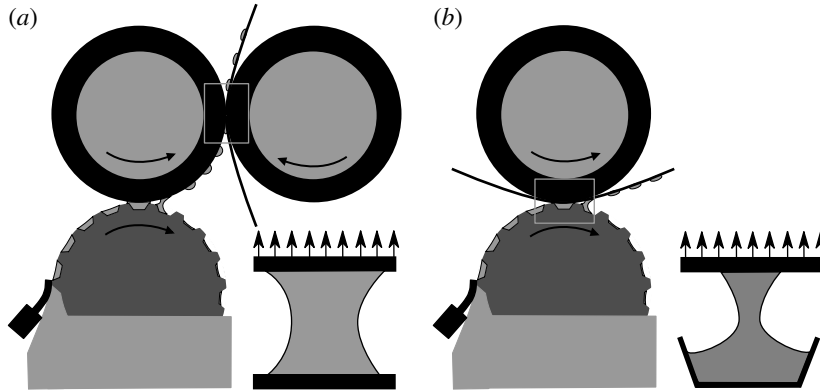


FIGURE 1. Sketches of gravure printing systems and their usual simplifications to model the liquid transference: (a) gravure offset and (b) direct gravure printing.

printing (Santa-Nokki *et al.* 2006; Ding *et al.* 2009). The high production rate and low manufacturing cost are crucial factors to compensate for the low-efficiency conversion these devices have at present (Krebs 2009). Other examples of electronic devices that can be manufactured by different printing technologies include flat-panel displays, which are formed by thousands of light emitting diodes (Chung *et al.* 2010; Lee *et al.* 2010b), and general purpose small-scale electronic circuits on flexible substrates (Pudas, Hagberg & Leppävuori 2004a,b; Lee *et al.* 2010a).

Among the many printing technologies used, gravure is very attractive because it allows the printing of small patterns (of the order of $10\ \mu\text{m}$) using liquids of medium viscosities (up to $1000\ \text{cP}$) at fast substrate velocities ($10\ \text{m s}^{-1}$ and higher) when a roll-to-roll configuration is used (Krebs 2009). The term gravure comes from the fact that one of the rolls has a pattern engraved on its surface, which is made of small cells or cavities. They are filled with liquid as the surface of the roll rotates inside a bath, then a blade removes the excess liquid and finally the cavities are emptied by direct contact, thereby transferring the engraved pattern to a second surface. As shown in figure 1(a), this second surface can be the surface of a rubber roll from which the pattern is later transferred to the substrate; this technique is known as offset gravure printing. In the other alternative, the pattern is transferred directly to the substrate by pressing the substrate between a rubber roll and the engraved cylinder itself (see figure 1b); in this case the technique is simply called gravure printing.

The liquid transfer process from individual cells or grooves to the surface of a roll is quite complex; it involves stretching of liquid bridges with moving contact lines. In addition, a detailed description of the complete problem involves consideration of the hydrodynamic effects between multiple cavities, and fluid–structure interaction aspects when deformable rolls are used. Thus, strong simplifications are usually made to build theoretical models and to understand the fundamental aspects of the problem. The most common one is to analyse the dynamics of just one isolated liquid bridge. Even the dynamics of a single liquid bridge, from its formation and evolution to its final breakup, requires the physics of free surfaces and moving contact lines, a deep understanding of which remains a considerable challenge in the field of fluid mechanics, although they have been active areas of research for the last four decades (Huh & Scriven 1971; Weinstein & Ruschak 2004; Blake 2006; Snoeijer & Andreotti 2013).

The simplest flow model to study liquid transfer in offset gravure printing is the stretching of a planar or axisymmetric liquid bridge between two flat surfaces. This problem is crucial to an understanding of printing applications and, maybe because of its simple geometry, it has been the problem most frequently considered (Gupta *et al.* 2007; Huang *et al.* 2008; Dodds, Carvalho & Kumar 2009; Kang *et al.* 2009; Dodds, Carvalho & Kumar 2011, 2012).

In order to model the liquid transfer from a cavity to a surface, the usual simplification is to consider the stretching of planar or axisymmetric liquid filaments between a moving surface (flat plate) and a fixed cavity. The main goal of such analyses is usually to determine the mass fraction of liquid that is transferred from the cavity to the moving surface (usually called the pick-out fraction and denoted as ϕ) as a function of contact angles, surface velocity, geometry of the cavity and flow parameters. One of the first numerical studies was conducted by Powell, Savage & Guthrie (2002), who used the finite element method to study the stretching of planar two-dimensional (2-D) liquid bridges between a trapezoidal cavity and a plate. They included inertial and gravitational effects in their analysis, but as a further simplification they considered that the contact lines on the plate were fixed, which certainly is not the case in printing processes. They found that the size of the sessile drop formed on the moving plate is slightly reduced when the stretching velocity is increased, while a more elongated liquid filament is obtained. More recently, Hoda & Kumar (2008) used the boundary integral method to study the removal of liquid from 2-D planar grooves with rectangular cross-sections. By simultaneously imposing shear (horizontal) and stretching (vertical) velocities to the upper plate, the authors predicted the residual liquid fraction left in the cavity for different cavity aspect ratios and stretching velocities. They also explored the effects of contact angles, but only for non-wetting conditions because of limitations in their numerical approach. The results show that almost all the liquid inside the cavity can be removed when the stretching velocity is higher than a critical value, which is a function of the cavity aspect ratio. The predictions also indicated that wider cavities are easier to empty. Huang *et al.* (2008) also analysed the stretching of a liquid bridge between plates and 2-D planar trapezoidal cavities, using the volume-of-fluid method to solve the free boundary problem. They explored the effect of wettability conditions on the width of the printed pattern at the plate, finding an expected strong influence of the contact angle at the plate contact line but a weak effect of the cavity wetting characteristics. Their results also show that the transferred liquid fraction falls slightly as the cavity wall is made steeper (at constant cavity depth). However, a strong decrease in pick-up fraction was observed as the depth of the cavity was augmented at constant wall slope.

Recently, Dodds *et al.* (2009) studied the behaviour of axisymmetric liquid bridges stretched between plates and cavities with trapezoidal cross-sections. They evaluated the liquid transfer fraction ϕ as a function of the cavity geometry, contact angles, initial condition and capillary number $Ca = \mu V / \sigma$ (where μ is the liquid viscosity, V is the reference velocity and σ is the surface tension). They used the Galerkin finite element method to solve the Stokes equations, and an elliptic mesh generation algorithm was used to map the physical and computational domains (Christodoulou, Kistler & Schunk 1997). The results show that ϕ rises with capillary number and as the cavity becomes wider.

Because of the inherent complexity in the visualization and measurement of such small-scale interfacial fluid flow, few experimental results are available; those of Yin & Kumar (2006) and Chuang, Lee & Liu (2008) are the exception. To simplify both

the visualization process and the measurements of the transferred liquid fraction, they upscaled engraved cavities to dimensions of the order of millimetres, much larger than the actual cavities used in gravure printing. More specifically, Yin & Kumar (2006) visualized the liquid transfer from a single large cell (of the order of 1 mm) to a curved surface that travelled horizontally over it. The experiments covered a wide range of capillary numbers, i.e. $10^{-4} < Ca < 5 \times 10^{-2}$, and they found that the pick-out liquid fraction diminishes from its maximum value close to $\phi = 0.5$ as the velocity of the moving surface is increased. Chuang *et al.* (2008) also used trapezoidal cells and made arrays of up to four cavities to study how their interaction affects the fraction ϕ . To better approximate the kinematics of a gravure printing process, they moved a roller at different velocities and gaps and studied the shape of the printed pattern over the roller and the remaining liquid left in the cells and the surface between them. Although the range of the capillary number explored was small ($2.5 \times 10^{-3} < Ca < 3 \times 10^{-2}$), the results also showed that the fraction ϕ falls as the capillary number rises.

A process closely related to gravure printing is the one used to coat thin uniform liquid films over moving substrates using rolls with engraved cells or grooves, called gravure coating. A more complete body of experimental results is available for gravure coating (see, for example, Pulkrabek & Munter 1983; Benkreira & Patel 1993; Kapur 2003). In particular, the work of Kapur (2003) indicates that the liquid extracted from cavities rises with capillary number in the range $10^{-2} < Ca < 10^{-1}$. However, despite their similarity, gravure printing and gravure coating present important differences which have a strong effect on the dynamics of the liquid transfer from the gravure roll cells to the smooth roll surface or substrate. In gravure coating, the liquid inside each cell is transferred to a continuous film coated on the substrate; in gravure printing, the fluid inside each cavity forms a liquid bridge that wets the substrate forming contact lines. Therefore, it is not clear how the pick-out fractions in gravure coating and gravure printing are related.

Summarizing, the available experimental results suggest that, in gravure printing, the transferred liquid fraction decreases as the capillary number rises, at least in the range explored. While the previous works of Hoda & Kumar (2008) and Huang *et al.* (2008) analysed the effect of contact angles and cavity shapes, all their results were obtained at a fixed capillary number, $Ca = 0.01$. Dodds *et al.* (2009) presented results for two values of the capillary number ($Ca = 0.1$ and 0.01), and their predictions suggest the opposite behaviour to that observed in the experiments: ϕ increases as the capillary number rises.

In the present work, we study the liquid transfer process from a fixed 2-D trapezoidal cavity to a moving plate. The analysis is made using a realistic kinematic description of the top-plate motion relative to the cavity, based on the kinematics of a roll-to-roll system (§ 2). This allows us to consider the stretching (vertical), shearing (horizontal) and rotational velocities in a coherent manner and to relate them to the operational parameter of the process. The relative motion between the two surfaces has a strong effect on the evolution of the contact line position and consequently on the liquid transfer process. We model the fluid flow by solving the Stokes equations with appropriate boundary conditions, which are presented in § 2. We implemented a robust numerical algorithm which is discussed in § 3. In § 4.2, we first compare the liquid transfer processes from axisymmetric and planar 2-D cavities. Then, we discuss the effect of the moving surface kinematics, cavity geometry and capillary number on the liquid transfer process. Finally, in § 5, we present the main conclusions of this work and future research directions.

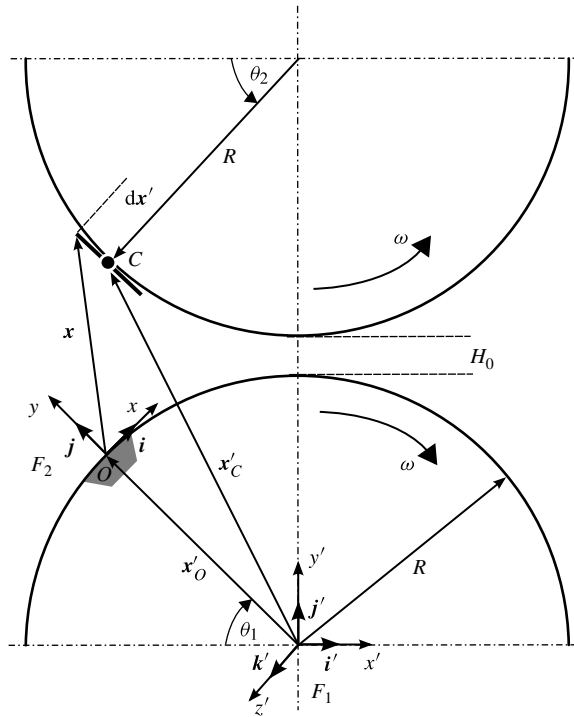


FIGURE 2. The geometric model, variables and frames used to describe the relative motion between the cavity and points on the top roll surface.

2. The model

2.1. Kinematic description of a rotational gravure printing system

Figure 2 shows the schematic configuration of two equal counter-rotating rolls separated by a gap H_0 . The positions of points on both roll surfaces are defined by the angles θ_1 and θ_2 with respect to the horizontal line, as shown in the figure. The bottom roll represents the engraved roll with the cavities; however, only one cavity is sketched (dark grey colour) to simplify the diagram. Figure 2 shows two frames of reference. One frame (F_1) is fixed at the centre of the bottom roll and is defined by the unit vectors ($\mathbf{i}', \mathbf{j}', \mathbf{k}'$). The coordinates of any point with respect to this frame are represented by (x', y', z') . The second frame of reference (F_2) is attached to the centre of the cell surface (point O) and therefore is moving with respect to the fixed frame of reference F_1 . The coordinates of any point with respect to the moving frame F_2 are represented by (x, y, z) . The goal is to derive an expression for the velocity \mathbf{V}_w of a point lying on a small plane rotating attached to the top roll (see figure 2) relative to the moving frame of reference.

The velocities of points C and O (located on the top and bottom roll surfaces, respectively) with respect to the fixed frame of reference F_1 are easily determined as

$$\left. \begin{aligned} \mathbf{V}'_C &= \omega R(\sin(\theta_2)\mathbf{i}' - \cos(\theta_2)\mathbf{j}'), \\ \mathbf{V}'_O &= \omega R(\sin(\theta_1)\mathbf{i}' + \cos(\theta_1)\mathbf{j}'), \end{aligned} \right\} \quad (2.1)$$

where $\theta_1 = \theta_2 = \omega t + \theta_0 = \theta$. The angle θ_0 allows one to consider an initial inclination or twist of the plate with respect to the cavity. However, this case will not be explored

in the present work and, for all cases analysed here, $\theta_0 = \pi/2$: points C and O are initially located in the minimum gap between the rolls. Because the size of the cavities ($\sim 10 \mu\text{m}$) is much smaller than the roll radius ($\sim 10 \text{ in.}$), the curvatures of both roll surfaces in the vicinity of C and O are neglected in the description presented here. The position of any point located on the top roll surface (in the vicinity of C) with respect to F_1 can be written as $\mathbf{x}' = \mathbf{x}'_C + d\mathbf{x}'$, where $d\mathbf{x}'$ is a vector tangent to the top roll surface through the point C . Therefore, the velocity of this point with respect to F_1 is

$$\mathbf{V}' = \mathbf{V}'_C + \omega'_C \times d\mathbf{x}' = \mathbf{V}'_C + \omega'_C \times [\mathbf{x}' - \mathbf{x}'_C], \quad (2.2)$$

where $\omega'_C = \omega_r \mathbf{k}'$ is the angular velocity at which $d\mathbf{x}'$ is rotating with respect to C . It is obvious that $\omega_r = \omega$, but soon it will be clear why we have introduced a different notation for this variable. The position vector \mathbf{x}'_C is given by $\mathbf{x}'_C = -R \cos(\theta) \mathbf{i}' + (2R + H_0 - R \sin(\theta)) \mathbf{j}'$.

From basic kinematics (see, for example, Lai, Rubin & Krempl 1999), the expression for the velocity of a point on the top roll surface (in the vicinity of C) with respect to frame F_2 is

$$\mathbf{V}_w = \mathbf{V}' + \mathbf{V}'_O - \omega'_O \times \mathbf{x}, \quad (2.3)$$

where \mathbf{V}'_O and ω'_O are the translational and rotational velocities of frame F_2 (which is attached to the point O) with respect to F_1 , respectively, and \mathbf{x} is the position vector $\mathbf{x}'_C + d\mathbf{x}'$ with respect to F_2 . Thus,

$$\mathbf{V}'_O = \omega R (\sin(\theta) \mathbf{i}' + \cos(\theta) \mathbf{j}'), \quad \omega'_O = -\omega_r \mathbf{k}'_O = -\omega'_C, \quad \mathbf{x} = x \mathbf{i} + y \mathbf{j}. \quad (2.4a,b,c)$$

By recognizing that $\mathbf{x}' = \mathbf{x}'_O + \mathbf{x}$, $\mathbf{x}'_O = -R \cos(\theta) \mathbf{i}' + R \sin(\theta) \mathbf{j}'$ and introducing the expression (2.2) for \mathbf{V}' in \mathbf{V}_w it follows that

$$\mathbf{V}_w = \mathbf{V}'_C - \mathbf{V}'_O + 2\omega'_C \times \mathbf{x} - \omega'_C \times [\mathbf{x}'_C - \mathbf{x}'_O]. \quad (2.5)$$

Because \mathbf{V}_w represents the velocity relative to the moving frame F_2 , it must be expressed in terms of its corresponding versors \mathbf{i} and \mathbf{j} , which are related with those of the fixed frame F_1 by $\mathbf{i}' = \mathbf{i} \sin(\theta) - \mathbf{j} \cos(\theta)$ and $\mathbf{j}' = \mathbf{i} \cos(\theta) + \mathbf{j} \sin(\theta)$. Then, replacing all quantities in (2.5), the final expression for the velocity of any point on the top roll surface (near C) with respect to the frame F_2 is given by

$$\mathbf{V}_w(\mathbf{x}, t) = \left. \begin{aligned} &[-2\omega R \cos^2(\theta) - 2\omega_r y + \omega_r y_C] \mathbf{i} + [-2\omega R \cos(\theta) \sin(\theta) + 2\omega_r x - \omega_r x_C] \mathbf{j}, \\ &x_C = |\mathbf{x}'_C - \mathbf{x}'_O| \cos(\theta), \quad y_C = |\mathbf{x}'_C - \mathbf{x}'_O| \sin(\theta), \\ &|\mathbf{x}'_C - \mathbf{x}'_O| = 2R + H_0 - 2R \sin(\theta). \end{aligned} \right\} \quad (2.6)$$

As mentioned before, all cases discussed here consider that the initial condition is such that the cavity and substrate are in the horizontal position ($\theta = \pi/2$). From this initial condition, the top roll surface evolves according to (2.6), while the cavity remains fixed. It is clear that the resulting kinematics given by (2.6) is a combination of the shear (horizontal), extension (vertical) and rotational velocities of the plate. It is important to mention that in the axisymmetric analysis, only the stretching or vertical velocity is considered in order to satisfy the assumed axial symmetry. For these cases, an alternative expression for the plate velocity, V_w , is used in which the shear and rotational velocities are neglected,

$$\mathbf{V}_w(\mathbf{x}, t) = -2\omega R \cos(\theta) \mathbf{j}. \quad (2.7)$$

The expression (2.7) should be considered as a limiting case of (2.6) as the sizes of the cavity and plate relative to the roll radius approach zero, making the rotational effects negligible, i.e. $\omega_r \sim 0$. Because $\theta \sim \pi/2$ and thus $\cos^2(\theta) \ll \cos(\theta) \sin(\theta)$, finally (2.6) simplifies to (2.7).

Another important issue to be considered here is the selection of the velocity scale for the problem. As was discussed by Dodds (2011), one is tempted to select the tangential roll surface velocity $V_t = \omega R$ as the velocity scale. However, because the cavity and plate surfaces have the same tangential velocity, V_t does not represent a correct scale at all. A more appropriate velocity scale is the stretching vertical velocity at which those surfaces are separating. It can be shown that this vertical velocity scale is given by $V_E = V_t \sqrt{2(L_b/R - (L_b/R)^2)}$ (Dodds 2011). In the above expression, L_b represents the breakup length, i.e. the vertical distance between the plate and cavity at which the liquid filament breaks. Simulations performed in both Dodds *et al.* (2009) and this work show that $L_b \sim 5\delta$, where δ is the depth of the cavity. Typical values of the above magnitudes in gravure printing systems are $V_t = 10 \text{ m s}^{-1}$, $\delta = 10 \text{ }\mu\text{m}$ and $R = 10 \text{ in} = 0.254 \text{ m}$. Thus, $V_E \sim V_t \sqrt{10\delta/R} \sim 0.2 \text{ m s}^{-1}$, that is, two orders of magnitude smaller than V_t . Then, by selecting V_E , δ and δ/V_E as scales of velocity, length and time, respectively, the dimensionless expressions for the plate velocity are

$$\mathbf{V}_w(\mathbf{x}, t) = -2\omega_b R_b \cos(\theta) \mathbf{j} \quad (2.8)$$

for pure stretching and

$$\mathbf{V}_w(\mathbf{x}, t) = [-2\omega_b R_b \cos^2(\theta) - 2\omega_p y + \omega_p y_C] \mathbf{i} + [-2\omega_b R_b \cos(\theta) \sin(\theta) + 2\omega_p x - \omega_p x_C] \mathbf{j} \quad (2.9)$$

for the general case (complete kinematics).

In the above expression, \mathbf{V}_w , x , y , x_C , y_C and $\theta = \omega_b t + \theta_0$ are dimensionless quantities; moreover, $w_b = \omega \delta / V_E$, $\omega_p = \omega_r \delta / V_E$ and $R_b = R / \delta$.

2.2. Flow equations and boundary conditions

The differential equations and the appropriate boundary conditions that describe the transient free surface flow with contact lines in the liquid transfer process are presented in this section. The flow domain and the relevant geometric parameters are shown in figure 3. The geometry in the figure represents (i) the cross-section of an axisymmetric cavity or (ii) the cross-section of a groove (also called a plane cavity in this work). Both configurations are used in gravure printing. Any complex pattern can be printed using an appropriate number and configuration of dots, placed sufficiently close to achieve the desired merging between the individual printed dots. However, when continuous patterns are printed, such as tracks of an electronic circuit, the transference of liquid from a groove engraved in the gravure rolls may lead to more uniform and continuous printing patterns (see, for example, Pudas *et al.* 2004a,b; Lee *et al.* 2010a,b).

The flow domain consists of a liquid bridge of a Newtonian liquid with density ρ , viscosity μ and surface tension σ , attached to the cavity and top plate. The surrounding gas phase has negligible density and viscosity (relative to the liquid properties) and a constant pressure $p_0 = 0$ which is set as reference. At $t = 0$ we consider the system to be in equilibrium, then the free surface is a static meniscus between the cavity and the plate with static contact angles θ_c and θ_p , respectively. The quantities \mathbf{x}_c^i and \mathbf{x}_p^i represent the contact line positions along the cavity and plate respectively, with $i = l$ denoting the left and $i = r$ the right contact lines. For

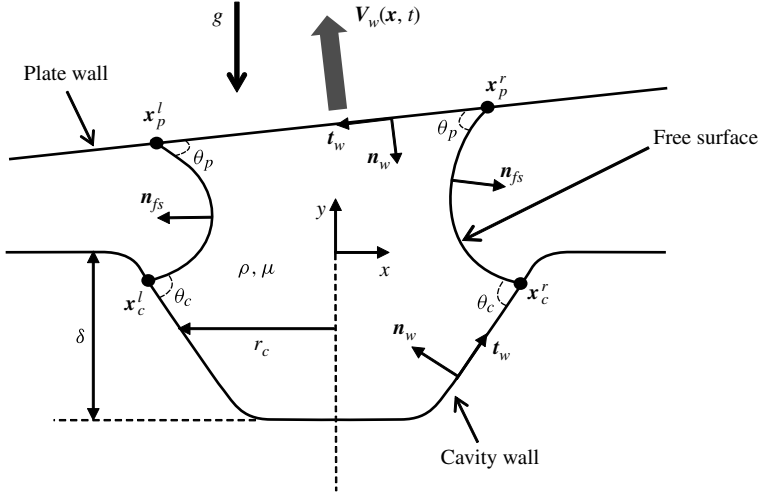


FIGURE 3. Sketch of the domain and geometric parameters. When the axisymmetric model is solved, x and y represent the radial and axial coordinates, respectively. For this particular case, the upper plate is always in the horizontal position and it moves only with vertical velocity.

the axisymmetric case, x_p and x_c collapse into a single circular contact line on each surface.

Using the dimensionless variables defined in the preceding section, we can estimate the values of the Reynolds number ($Re = \rho \delta V_E / \mu$) and the Stokes number ($St = \rho g \delta^2 / (V_E \mu)$). In gravure printing applications, the cavity depth is of the order of $10 \mu\text{m}$, the liquid viscosity is usually between 1 and 100 cP and the extensional velocities are between 1 and 10 cm s^{-1} ; therefore, $10^{-3} < Re < 1$ and $10^{-5} < St < 10^{-1}$. Thus, while the gravity forces can be safely neglected, the inertial effects could be important in some situations. However, to maintain the present model as simple as possible, we also neglect the inertial effects and thus the momentum and mass conservation equations are

$$\left. \begin{aligned} \nabla \cdot \mathbf{T} &= 0, \\ \nabla \cdot \mathbf{v} &= 0. \end{aligned} \right\} \quad (2.10)$$

In (2.10), $\mathbf{T} = -p\mathbf{I} + (\nabla \mathbf{v} + \nabla \mathbf{v}^T)$ is the total stress tensor (\mathbf{I} is the identity tensor), made dimensionless with $V_E \mu / \delta$.

We consider the liquid surface tension to be constant and, therefore, the capillary force along the interface has only a normal component, given by

$$\mathbf{n}_{fs} \cdot \mathbf{T} = \frac{\kappa}{Ca} \mathbf{n}_{fs}, \quad (2.11)$$

where $Ca = \mu V_E / \sigma$ is the capillary number and κ is the mean curvature of the free surface ($\kappa = -\nabla_s \cdot \mathbf{n}_{fs}$). In the above expression, $\nabla_s = (\mathbf{I} - \mathbf{n}\mathbf{n}) \cdot \nabla$ is the surface gradient operator.

The moving plate and cavity surfaces are impermeable and because the contact lines slip along them, we must introduce some approximation to overcome the stress singularity at the contact lines (Huh & Scriven 1971). As in Dodds *et al.* (2009),

Navier's slip boundary condition is used and a prescribed constant contact angle between the liquid interface and solid walls is imposed,

$$\left. \begin{aligned} \mathbf{v} \cdot \mathbf{n}_w &= 0 & \text{at the cavity walls,} \\ (\mathbf{v} - \mathbf{V}_w) \cdot \mathbf{n}_w &= 0 & \text{at the moving plate,} \end{aligned} \right\} \quad (2.12)$$

$$(\mathbf{n}_w \cdot \mathbf{T}) \cdot \mathbf{t}_w = 1/\beta(\mathbf{t}_w \cdot (\mathbf{v} - \mathbf{v}_{surf})), \quad \mathbf{n}_w \cdot \mathbf{n}_{fs} = \cos(\theta_i), \quad i = c, p. \quad (2.13a,b)$$

In (2.13), β is the dimensionless slip coefficient (as defined in Lamb 1975), \mathbf{v}_{surf} is the velocity of the solid surface and θ_i is the macroscopic dynamic contact angle, which, for simplicity, we consider to be constant. We could have used a more sophisticated approach to model the contact line by introducing, for example, a dependence of the apparent dynamic contact angle on the velocity. Blake (2006) discuss the different available models. However, we decided to use a simple approach given by (2.13), to focus our analysis on the effects of the top-plate kinematics and capillary number on the system.

Because the above flow equations and boundary conditions must be solved in a domain that is moving and deforming, the domain itself is part of the solution. A convenient way to solve free boundary problems is to map the unknown physical domain to a reference computational domain. The mapping is constructed by considering the domain as a fictitious elastic solid which deforms in response to boundary loading. Following Cairncross *et al.* (2000), the position of the interior nodes of the domain obeys a quasi-static equilibrium equation,

$$\left. \begin{aligned} \nabla \cdot \mathbf{S} &= 0, \\ \mathbf{S} &= \lambda_s e \mathbf{I} + 2\mu_s \mathbf{E}, \end{aligned} \right\} \quad (2.14)$$

where \mathbf{S} is the Cauchy stress tensor of the pseudosolid, which is related to the deformation field through a Hookean constitutive equation. In (2.14), λ_s and μ_s are the Lamé constants of the pseudosolid, \mathbf{E} is the Eulerian strain tensor and e is the volume strain. One important aspect of the mapping introduced by Cairncross *et al.* (2000) was the use of a finite Eulerian strain tensor

$$\mathbf{E} = \frac{1}{2} [\nabla \mathbf{d} + \nabla \mathbf{d}^T - \nabla \mathbf{d} \cdot \nabla \mathbf{d}^T] = \frac{1}{2} [\mathbf{I} - \mathbf{F}^{-T} \mathbf{F}^{-1}], \quad (2.15)$$

where $\mathbf{d} = \mathbf{x} - \mathbf{X}$ is the displacement field, \mathbf{x} represents the current coordinates of the nodes at time t (to be calculated), \mathbf{X} represents the coordinates of the fixed free-stress reference state and $\mathbf{F} = \partial \mathbf{x} / \partial \mathbf{X} = \mathbf{I} + \partial \mathbf{d} / \partial \mathbf{X}$ is the Lagrangian deformation gradient with respect to the undeformed reference state. Finally, the volume strain is $e = 3(\det(|\mathbf{F}|^{1/3}) - 1)$, which reduces to $\text{tr}(|\nabla \mathbf{d}|)$ for small displacements.

To solve (2.14) two types of boundary conditions are used. The first is a kinematic condition that links the velocity of the computational nodes with the velocity of the fluid particles. This boundary condition is used along moving surfaces, such as the interface and the moving plate, i.e.

$$\left. \begin{aligned} \mathbf{n}_{fs} \cdot (\mathbf{v} - \dot{\mathbf{x}}) &= 0 & \text{at free surfaces,} \\ \mathbf{n}_w \cdot (\mathbf{v} - \dot{\mathbf{x}}) &= 0 & \text{at the moving plate.} \end{aligned} \right\} \quad (2.16)$$

In the above expressions $\dot{\mathbf{x}}$ represents the velocity of the computational nodes and \mathbf{v} the fluid velocity on that boundary. The second type of boundary condition imposed

on (2.14) is an equation that describes the mesh displacements themselves, instead of the nodal velocities. These boundary conditions are applied on nodes located along the symmetry axis (in the case of axisymmetric solutions) and cavity walls. Along the symmetry axis, $(\mathbf{x} - \mathbf{X}) \cdot \mathbf{n} = \mathbf{d} \cdot \mathbf{n} = 0$. The coordinates of the nodes on the cavity wall must satisfy (Dodds *et al.* 2009)

$$y = f(x) = -\frac{1}{2} \left[1 - \tanh \left(\frac{|x| - r_c}{r_s} \right) \right] \quad \text{along the cavity wall.} \quad (2.17)$$

In (2.17), r_c is the width of the cavity, measured at $y = -\delta/2$ (in dimensional units). In addition, r_s is a parameter that controls both the curvature of the corners and the steepness of the cavity wall. Sharp corners and steep cavity walls are obtained using small values of r_s . All quantities in (2.17) are made dimensionless with the cavity depth δ .

3. Numerical solution

The numerical technique used in this work is similar to procedures that have been used successfully to solve other fluid flow problems involving interfacial dynamics. The main ideas were taken from the works of Cairncross *et al.* (2000), Sprittles & Shikhmurzaev (2012) and Ubal *et al.* (2012), in which detailed descriptions of the numerical features were given. Different numerical approaches discussed in the aforementioned works were combined here to construct a robust numerical procedure; they are briefly described in this section.

The flow domain was divided into elements using an unstructured mesh of triangles. All boundary conditions were enforced using Lagrange multipliers, as described in Sprittles & Shikhmurzaev (2012) and Ubal *et al.* (2012). Biquadratic interpolating functions were used to expand the velocity, pseudosolid displacement (nodal coordinates) and the Lagrange multipliers associated with each boundary condition; bilinear continuous basis functions were used to expand the pressure field (six-node P2P1 Taylor–Hood triangular elements).

An implicit second-order time integration scheme with an adaptive time step was used. At each time step, all variables were calculated simultaneously. This fully coupled scheme shows better convergence and stability properties compared with other decoupled or semi-implicit numerical procedures (Christodoulou & Scriven 1992; Campana *et al.* 2007). The resulting set of nonlinear equations at each time step was solved using Newton's method.

The model was implemented in the commercial finite element software COMSOL Multiphysics (COMSOL Multiphysics 1998–2013) and the approximated solutions were obtained following the steps described next. First, an initial guess for the flow domain was built using CAD tools; we denote this initial domain (or geometry) as G_0 . It approximates the shape of the cavity, the plate and the static liquid bridge connecting them. This initial domain was meshed (M_0) and the coordinates of the nodes were taken to be the initial reference state X_0 for the pseudosolid deformation equation. The second step consisted of solving the mesh deformation equation alone with the reference state X_0 . The mesh evolved through successive iterations until it accurately described the cavity geometry (see (2.17)). The new mesh M_1 generated by the converged solution of the previous step was used to build a new geometry G_1 and to define the new reference state X_1 . In the third step, the true steady-state solution, i.e. the static configuration of the liquid bridge, was obtained. The full

set of differential equations (2.10) and (2.14) with their corresponding boundary conditions was solved setting the plate velocity (V_w) equal to zero; in this step the free surface evolved until it reached the static meniscus configuration. Then, the converged solution was used to define a new flow domain G_2 , which was remeshed (M_2) to get high-quality elements and a new reference state X_2 . Finally, the mesh M_2 , the reference state X_2 and the converged flow field solution were used as initial guesses for the transient calculations considering the moving plate (V_w given by (2.6) or (2.7)). This procedure was repeated for each different cavity geometry.

The element size in different regions of the flow domain was controlled to ensure the accuracy of the solution. Special care was taken near the contact lines and regions of high interface curvature. Near the contact lines, the difference between the computed θ_c and the imposed contact angle θ ($\Delta\theta = |\theta - \theta_c|$) was used as a measure of the solution accuracy, as suggested by Sprittles & Shikhmurzaev (2012). The element size near the contact line was adjusted during the computations, such that $\Delta\theta_{max} \sim 3\%$. Apart from controlling the element size near the contact line, several mesh tests were also performed to verify that the solutions presented were mesh-independent.

As the liquid bridge is highly deformed during the liquid transfer process, the elements become distorted, compromising the solution accuracy. To control the whole mesh, the aspect ratio of each element is computed during the transient calculation. Whenever this control parameter goes below a critical value, the liquid bridge configuration of the last converged solution is used to define a new geometry (and reference state), which is tessellated into a new high-quality mesh of triangles. The last converged solution is interpolated onto the new mesh and the time integration resumes. Typically, the simulations presented here required between nine and 14 stages of remeshing before achieving the breakup time. There is an inherent error in each geometry reconstruction and further remeshing procedure. The total volume of the liquid bridge was used as a control variable to verify the error associated with the remeshing and interpolation steps. The maximum total variation between the initial and breakup times was always below to 0.1% (in most cases it was approximately 0.01%).

We tested several iterative solvers and preconditioners built-in in COMSOL Multiphysics[®] but the convergence was very slow or was never achieved. Thus, we solved the linear system for each Newton's iteration using a direct solver, i.e. PARDISO (Schenk & Gärtner 2004), which ensured converged solutions in three or four Newton's iterations when using an appropriate initial guess.

4. Results

4.1. Validation and selection of a base case

We first validate the proposed model and its implementation by comparing the predictions with the axisymmetric results presented by Dodds *et al.* (2009). However, it is important to note that there are some basic differences between the two models that may lead to small discrepancies in the results. Dodds *et al.* (2009) imposed slip only on the nodes located at contact lines, while a no-slip condition was imposed on the remaining nodes located along the solid walls. Since they used a very large value for the slip coefficient, i.e. $\beta = 10^{10}$, this means that perfect slip (zero shear rate) was imposed at the contact lines. In contrast, the model used here considers Navier slip along the entire wall, and away from the contact line (outside the slip region) the tangential velocity approaches zero, i.e. $O(10^{-4})$. Thus, the size of the region

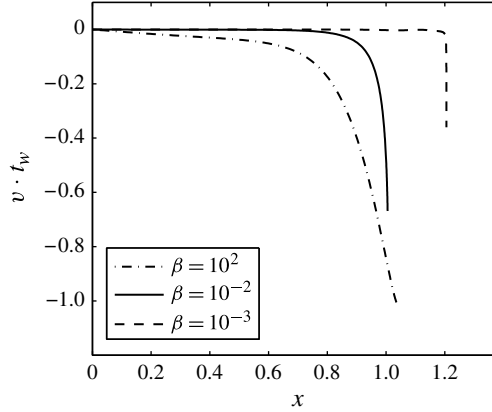


FIGURE 4. The tangential velocity on the cavity wall at $t = 0.1$ for the simulations of figure 5.

close to the contact line at which slip is significant and the value of the contact line velocity depend on the magnitude of the slip coefficient. Therefore, our results are more sensitive to the prescribed value of β . The slip coefficient β can be estimated based on the slip length l , i.e. $\beta \sim l/\delta$. Considering $l \sim 1\text{--}10$ nm, the slip coefficient should be $10^{-4} < \beta < 10^{-3}$. The range explored in the analysis was expanded to consider the limiting case of the high-slip condition ($\beta = 100$). However, values of $\beta > 10^{-2}$ lead to unrealistic large-slip regions. The predicted volume transfer ϕ from an axisymmetric cavity to a plate moving vertically reproduced the values reported by Dodds *et al.* (2009) for $10^{-2} < \beta < 10^{-3}$.

Before presenting the results of the parametric study, a base case (BC) was analysed to discuss the important phenomena that occur during the liquid transfer process. The BC parameters were chosen considering typical values of the operating conditions, geometric parameters and liquid properties. By taking $\mu = 0.01$ Pa s, $\sigma = 0.05$ N m $^{-1}$, $R = 6$ in = 0.1524 m, $\delta = 10$ μ m, $V_w = 10$ m s $^{-1}$, the corresponding dimensionless parameter values are $R_b = 15240$, $\omega_b = 0.0025$, $Ca = 0.05$. For simplicity we have set $Ca = 0.1$ and have neglected inertia ($Re = 0$). In the BC, the cavity geometry parameters were chosen as $r_c = 0.8$ and $r_s = 0.3$ and the contact angles were set as $\theta_c = \theta_p = 70^\circ$ (Dodds *et al.* 2009).

The initial gap H_0 between the plate and the top boundary of the cavity ($x = 0$) is also a parameter and it was set to $H_0 = 0.03$ for all cases. This a reasonable value to avoid extremely thin gaps at initial times and also to avoid contact between the plate and the cavity corner when the plate is under rotation. Because we cannot follow the evolution up to the filament breakup itself, a termination criterion for the simulation was defined. The runs were stopped when the minimum bridge thickness was less than 0.03 and this instant was taken to be the breakup time t_b .

Figure 4 shows the tangential velocity along the cavity wall at $t = 0.1$ for different values of β . The plot shows the unrealistic large-slip length for $\beta > 10^{-2}$. The interface configuration at breakup as a function of β is shown in figure 5. Clearly, the dynamics of the contact line motion has a strong effect on the liquid transfer process. Henceforth, all the predictions presented were obtained using realistic values of the slip coefficient, $\beta = 10^{-3}$ ($l = 10$ nm).

Table 1 summarizes the parameters of the BC.

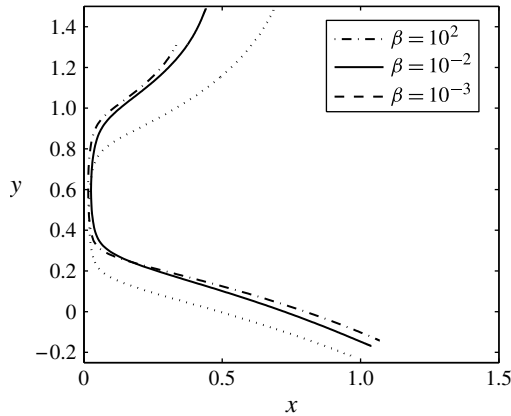


FIGURE 5. The free surface at breakup time for an axisymmetric cavity ($r_c=0.8$, $r_s=0.3$), $Ca=0.1$ and $\theta_c=\theta_p=70^\circ$.

Ca	$\theta_p=\theta_c$	β	r_c	r_s	R_b	H_0	$\omega_b=\omega_p$	θ_0
0.1	70°	10^{-3}	0.8	0.3	15240	0.03	2.5×10^{-3}	90°

TABLE 1. Values of the model parameters corresponding to the BC.

4.2. The case of pure stretching

First, the case in which the top plate is moving vertically above the cavity is analysed and the plate kinematics is defined by (2.7). The main goal of this analysis is to compare the flow during the liquid transfer process from an axisymmetric cavity (used to print a dot) and a 2-D groove (used to print a line). While axisymmetric cavities are difficult to find in real applications, they serve as a simplified model of more realistic trapezoidal cavities (see, for example, Chuang *et al.* 2008). In contrast, planar cavities or grooves are used to print circuit tracks (see, for example, Pudas *et al.* 2004a,b; Lee *et al.* 2010b).

As discussed by Dodds *et al.* (2009), there are two inherent time scales in the stretching of liquid bridges between plates and axisymmetric cavities. At the beginning of the process, the time scale is controlled by the movement of the contact line on the cavity wall which mainly depends on the cavity geometry, the contact angle and the slip parameter (wettability conditions). At later stages, the time scale is defined by the dynamics of the liquid bridge thinning process. The azimuthal curvature completely dominates the force balance along the interface, producing a high-pressure region in the neck that accelerates the breakup. In contrast, if the axisymmetric cavity is replaced by a planar groove, the absence of the azimuthal curvature delays the breakup. However, at the beginning of the emptying the behaviour cannot be so directly inferred. Thus, in the following we focus the analysis on this aspect of the problem.

Figure 6 compares the liquid transfer from an axisymmetric cavity (dashed line) and a groove (continuous line) by showing the evolution of the interface configuration up to the breakup time t_b . Starting from nearly the same quasi-static meniscus, the differences in the interfacial configurations are remarkable. For the axisymmetric case, the pressure on the liquid side of the interface is negative from $t=0$ up to $t \sim 3.5$

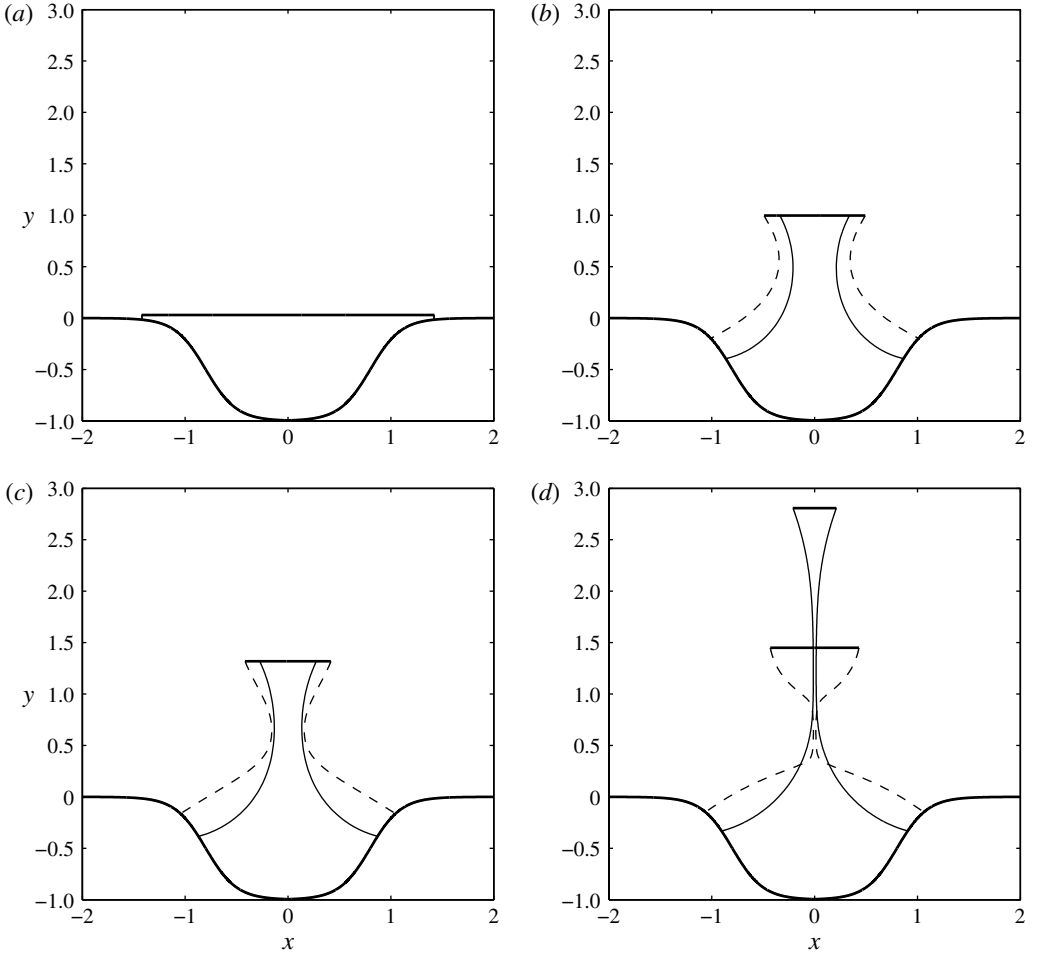


FIGURE 6. The free surface evolution during the emptying of the axisymmetric cavity (dashed line) and the groove (continuous line), for the BC and for pure stretching: (a) $t=0$, (b) $t=3.11$, (c) $t=3.59$, (d) the breakup time is $t_b=3.76$ for the axisymmetric cavity and $t_b=5.27$ for the groove.

because the azimuthal curvature is smaller than the curvature in the tangent direction. However, for $t > 3.5$, the effect of the azimuthal curvature is more pronounced and the pressure becomes positive. The neck of the bridge is the region with higher pressure and consequently the fluid is quickly drained towards both the plate and the cavity, producing the breakup at $t_b = 3.76$. It should be noted that at this instant the free surface near the cavity has a convex shape that is also observed in the results presented by Dodds *et al.* (2009). In contrast, for the groove, when the filament is elongated the curvature diminishes and, consequently, the pressure gradient that drives the liquid drainage falls. Thus, the thinning at the neck is only promoted by the stretching itself and the breakup is achieved later ($t_b = 5.27$). As a consequence, at t_b the plate is at $y \sim 2.8$, nearly twice the height reached in the axisymmetric case.

The changes in the liquid pressure related to the interface curvature have a strong effect on the pressure gradient at the contact lines and, consequently, on the contact

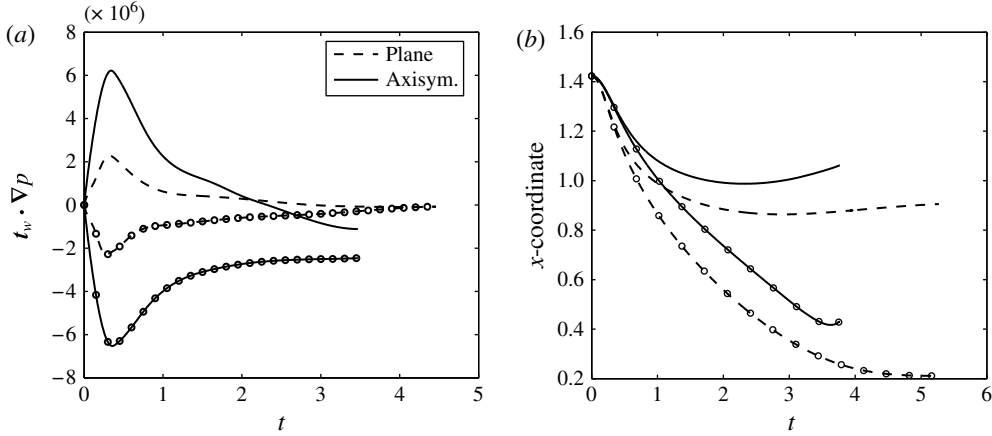


FIGURE 7. Contact line mobility represented by (a) its tangential pressure gradient and (b) its x -coordinate versus time. The curves with circles correspond to the contact lines on the moving plate.

line mobility. Figure 7(a) depicts the evolution of the pressure gradient in the direction tangent to the solid wall near the right contact lines (plate and cavity); i.e. $dp/ds = t_w \cdot \nabla p$ for both axisymmetric and plane geometry. It is important to note that, as shown in figure 3, the tangent vector t_w points towards the contact line on the cavity and away from the contact line on the plate. Therefore, although $t_w \cdot \nabla p$ has different signs along the plate (line and markers) and the cavity (line), the pressure falls along both surfaces as one moves away from the contact lines. These results should be interpreted only as an approximation to the pressure gradient which depends, in the vicinity of the contact lines, on the discretization used in our computations. It is well known that by using Navier's slip model, the pressure gradient near the contact line should scale as $dp/dr \sim 1/r$, where r is the distance from the contact line. Therefore, dp/dr should be infinite at the contact lines (see, for example, Shikhmurzaev 2006).

Figure 7(b) shows the corresponding evolution of the x -coordinate of the contact line for both geometries. From the beginning of the liquid transfer until $t \sim 0.4$, the pressure gradient close to the contact lines quickly increases, leading to a high contact line velocity towards the symmetry axis $x=0$. Although the pressure gradient is higher for the axisymmetric geometry, the contact line mobility is lower, as is clear from figure 7(b). In the axisymmetric case a tangent displacement of the contact lines produces an associated change in the azimuthal interfacial perimeter. This additional liquid confinement results in a lower contact line mobility and, consequently, in a stronger contact line pinning.

As mentioned before, in this work the breakup is the time when the filament thickness reaches a threshold value. Like other authors (Powell *et al.* 2002; Dodds *et al.* 2009) we have also supposed that after the breakup, the volume of liquid contained between the section of minimum thickness and the plate (Φ_p) remains on the plate. Thus, we define $\phi = \Phi_p/\Phi_i$ as the fraction of liquid transferred to the plate, relative to the initial total volume Φ_i . For the axisymmetric geometry $\phi = 0.066$ and for the plane geometry $\phi = 0.12$. The smaller volume transferred in the axisymmetric geometry is a consequence of the stronger pinning effect and the shorter breakup time observed for this configuration. From a practical point of view, these results suggest

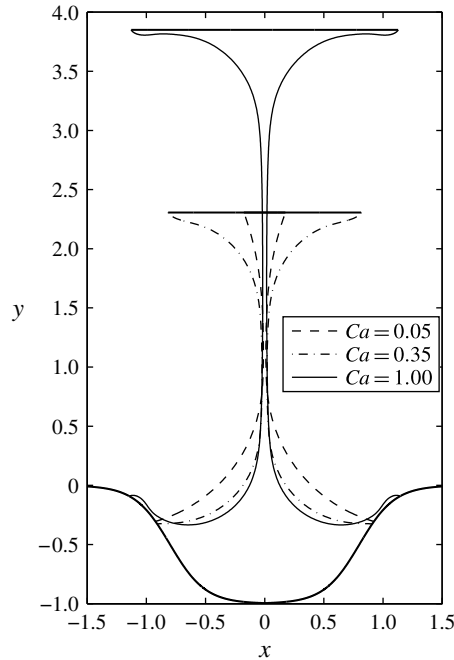


FIGURE 8. Free surface shapes for planar cavities, pure stretching motion and three values of Ca . The remaining parameters are those of the BC.

that planar cavities or grooves are easier to empty than cells. However, since a 2-D liquid filament can be significantly more elongated than an axisymmetric one, it can break up forming one or more satellite drops (see Huang *et al.* 2008), introducing inaccuracies in the printed pattern.

Dodds *et al.* (2009) showed that for axisymmetric cavities, the fraction ϕ increases with Ca , and we observed the same behaviour for planar cavities. The increase in the transferred volume fraction is directly associated with the contact line displacement. Figure 8 presents the interface configuration at the instant of filament breakup for three values of the capillary number. As explained by Dodds *et al.* (2009), the mobility of the contact lines depends on the capillary pressure gradient, which is a function of both the capillary number and the curvature gradient near the contact line (see (2.11)). At $Ca = 0.05$, the free surface reaches the corner of the cavity wall with an almost constant curvature, leading to a low-pressure gradient and consequently a strong pinning of the contact line. In contrast, the free surfaces at the plate show a higher curvature variation. Thus, while the cavity contact lines remain almost pinned, the plate contact lines move toward each other quickly, reducing the size of the drop formed on the plate. At $Ca = 0.35$, the mobility of the cavity contact lines is similar, but on the plate it is notably reduced due to the smaller pressure gradient. Therefore, a larger drop is formed on the plate following breakup, resulting in a significant increase of ϕ . It is interesting to note that the breakup is reached at almost the same plate-cavity separation for both $Ca = 0.05$ and $Ca = 0.35$. However, for $Ca = 0.35$ the capillary forces are weaker and the interface appears to be strongly curved. At $Ca = 1$ the viscous effects are large and the pressure gradient is small, resulting in a very strong pinning of all contact lines; consequently, the fraction ϕ is even higher. Because

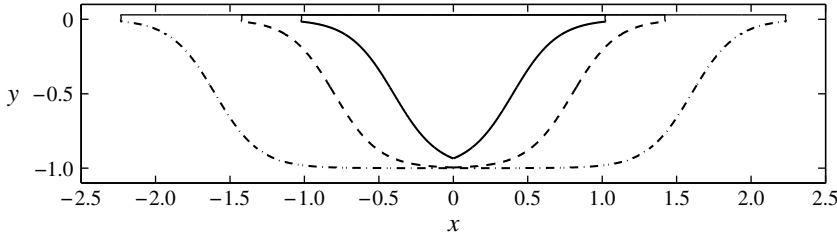


FIGURE 9. The cavity (groove) shapes used in this work: $r_c = 0.4$ (continuous), $r_c = 0.8$ (dashed) and $r_c = 1.6$ (dash-dotted). The top moving plate is in its initial horizontal position ($y = H_0 = 0.03$); the initial static menisci used to start the simulation are also shown.

of the very low interfacial rigidity, thin liquid films are formed in the vicinity of the cavity and plate contact lines.

In summary, the above results show that for both plane and axisymmetric cavities under pure stretching kinematics, the transferred liquid fraction increases with capillary number. In the next section we will show that this behaviour changes dramatically when shearing and rotation are included in the plate motion.

4.3. Effect of the cavity aspect ratio and roll radius

In this section we analyse the effect of the cavity width and roll size on the liquid transfer process, considering the full kinematics of a roll-to-roll system (see (2.9)). Because the plate motion now includes the combined effects of stretching, rotation and shearing, only 2-D plane cavities (grooves) are investigated. Predictions are shown for two values of the dimensionless roll radius, i.e. $R_b = 15\,240$ and 2540 . Considering a cavity depth $\delta = 10\ \mu\text{m}$, these values correspond to the roll radius, R , equal to 6 and 1 in., respectively. The first value is a typical roll radius in gravure printing systems, while the second is representative of microgravure printing applications (Lee *et al.* 2010b). As the roll radius R_b decreases, the curvature of the roll begins to be comparable to the cavity size and, consequently, the rotation and shear motion become more important. To evaluate this effect, three different cases were studied: (i) pure stretching motion with $R_b = 15\,240$, $\omega_b = 2.5 \times 10^{-3}$ and $\omega_p = 0$, as in the previous subsection (plate velocity given by (2.7)); (ii) full roll-to-roll kinematics (2.9) with $R_b = 15\,240$ and $\omega_p = \omega_b = 2.5 \times 10^{-3}$, and (iii) full roll-to-roll kinematics with roll radius $R_b = 2540$ and $\omega_p = \omega_b = 6.27 \times 10^{-3}$. Since ω_b and ω_p scale with $1/R_b^{1/2}$, the dimensionless rotation speed changes even though the dimensional rotation is fixed. Regarding the cavity aspect ratio, the values explored were $r_c = 0.4, 0.8$ and 1.6 , while r_s was kept constant at $r_s = 0.3$. The initial level of liquid at $t = 0$ was set at $H_0 = 0.03$ for all the conditions explored. This implies that the initial liquid meniscus between the plate and the cavity will be formed at different horizontal positions (x -coordinates) but at approximately the same position relative to the exterior corner, as illustrated in figure 9.

Figure 10 shows ϕ as a function of the parameter ω_p for different cavity sizes r_c . The results show that ϕ always increases with r_c , suggesting that wider cavities are easier to empty. The breakup of the liquid filament is controlled by two time scales. One is related to the initial filament thickness, because thicker filaments take more time to reach the breakup point. The other is the time required for the contact

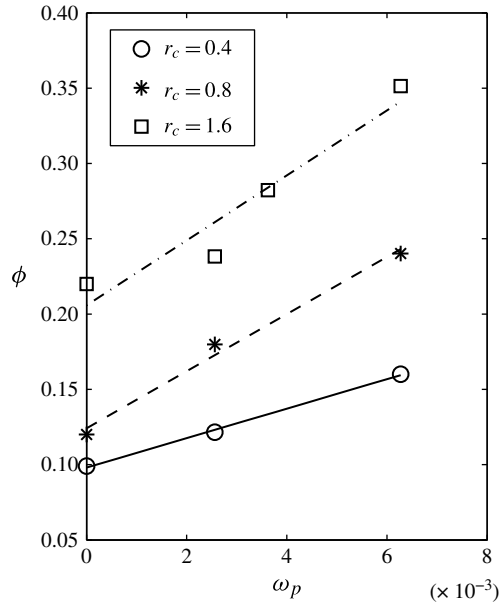


FIGURE 10. The liquid volume fraction transferred to the moving plate as a function of the kinematic parameter ω_p and the cavity (groove) aspect ratio.

lines to move along the cavity wall, which is related to the wettability properties, slip coefficient, contact angle and the slope and curvature of the wall. Since these properties and parameters were constant in our simulations, the breakup is only controlled by the initial thickness. Thus, a thicker initial filament (wider cavity) takes more time to thin, allowing the contact lines to move a longer distance inside the cavity before the breakup. As a result, more liquid can be removed from the cavity. Figure 11 depicts the free surfaces at the breakup for all cases presented in figure 10. The experiments on gravure coating presented by Kapur (2003) give strong physical evidence that the liquid fraction increases when wider cavities are used.

Results also show that for a fixed cavity geometry, the volume of liquid transferred to the plate increases with ω_p . Higher values of ω_p are associated with higher angular velocity and smaller roll radius. Figure 11 illustrates how the relative rotation and lateral displacement of the plate result in a non-symmetric motion of the contact lines when $\omega_p \neq 0$: while the left contact line moves outside the cavity, the right contact line goes deeper into it, leading to a more intense liquid displacement out of the cavity and consequently a delayed filament breakup. With a wide cavity ($r_c = 1.6$) the behaviour is not monotonic. The breakup at the higher value of ω_p ($\omega_p = 6.27 \times 10^{-3}$) occurred faster; consequently the plate position at the breakup is closer to the cavity. This early breakup can be explained by examining the evolution of the filament interface during the liquid transfer process, shown in figure 12 for the narrowest and widest cavities and $\omega_p = 6.27 \times 10^{-3}$. The effect of the plate rotation is stronger for the wide cavity because of the lateral separation of the free surfaces. The right contact line moves quickly inside the cavity. However, the left contact line stays more or less pinned at the cavity corner. Clearly, the contact line does not move rapidly enough to avoid a large deformation of the filament. However, in the small cavity (figure 12a), the contact lines move faster and smaller deformations are expected; the same occurs for $r_c = 0.8$.

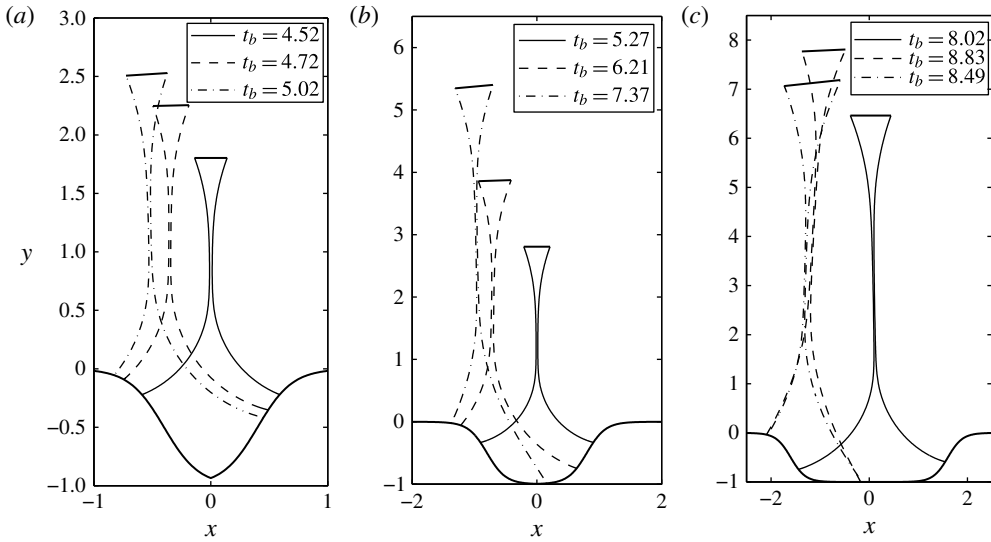


FIGURE 11. The free surfaces at breakup for the three cavity (groove) sizes: (a) $r_c = 0.4$, (b) $r_c = 0.8$ and (c) $r_c = 1.6$. On each graph, the solid line corresponds to $\omega_p = 0$, the dashed line to $\omega_p = 2.5 \times 10^{-3}$ and the dash-dotted line to $\omega_p = 6.27 \times 10^{-3}$.

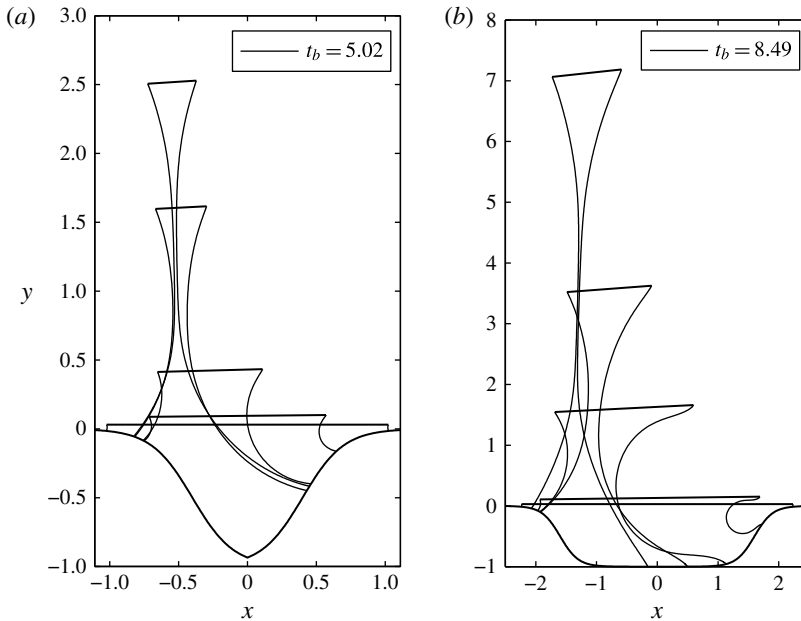


FIGURE 12. The free surface evolution during the emptying of a cavity (groove) with (a) $r_c = 0.4$, (b) $r_c = 1.6$ for $R_b = 2540$ ($\omega_r = 6.27 \times 10^{-3}$). The other parameters are those of the BC.

The width of the printed pattern, i.e. the distance between the two contact lines on the plate, in units of the cavity width, at breakup is presented in figure 13 as a function of cavity size (r_c) and angular velocity (ω_p). This result does not consider the

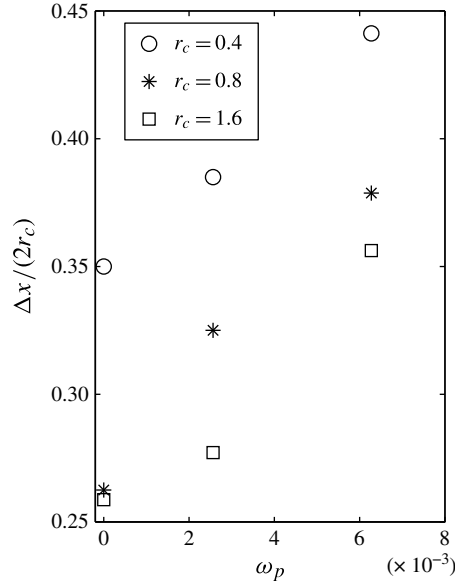


FIGURE 13. The width of the printed pattern on the substrate, normalized by the cavity (groove) width, versus the kinematic parameter ω_p and the cavity aspect ratio.

post-breakup flow of the liquid deposited on the substrate. The printed width increases as the rotational and shearing effects become stronger, i.e. higher values of ω_p . The longer breakup time observed with wide cavities leads to a greater reduction of the dimensionless printed width. For all cases analysed, the printed width varied from 0.25 to 0.45 of the cavity width.

4.4. Effect of Ca number

Gravure printing is used with liquids of very different viscosities and at different speeds. Therefore, it is important to determine how the dynamics of the liquid transfer process changes with the ratio of viscous to surface tension forces. The liquid fraction is plotted in figure 14 as a function of the capillary number and for the same parameters as reported in table 1. For comparison, the predictions for pure stretching ($\omega_p = 0$) and the experimental results obtained by Yin & Kumar (2006) and Chuang *et al.* (2008) are also included. Although these experimental results were obtained under kinematics and geometry conditions different from the cases simulated in this work, they are two of the few available results that discuss how the pick-out fraction varies with the capillary number in a liquid transfer process.

The predictions for pure extensional motion, i.e. $\omega_p = 0$, reveal a monotonic behaviour showing that ϕ rises with capillary number. This is the same behaviour as that reported by Dodds *et al.* (2009), who also assumed pure stretching kinematics. The predictions obtained with the complete roll-to-roll kinematics present a strong nonlinear behaviour, showing a local maximum and minimum. This complex behaviour of ϕ can be understood by analysing the evolution of the interfaces up to breakup for each particular case, as shown in figure 15. The sequence of interfacial configurations for each case does not correspond to the same instant of time; the particular sequence for each case was selected to better describe the evolution of the interface deformation and contact line motion.

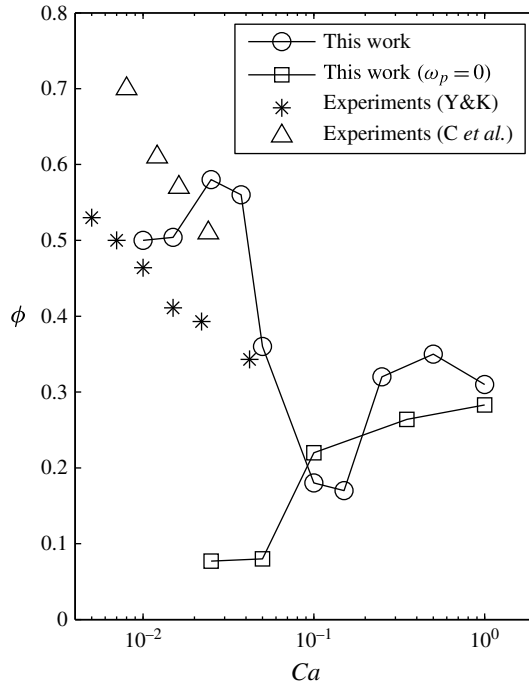


FIGURE 14. The mass fraction transferred to the substrate versus the capillary number Ca . The other parameters correspond to the BC (table 1). Y & K: experiments by Yin & Kumar (2006). C *et al.*: experiments by Chuang *et al.* (2008).

The interface evolution for $Ca = 0.01$ is presented in figure 15(a). Because of the plate rotation, the radius of curvature of the left meniscus is smaller than the radius of curvature of the right interface. The curvature difference sets a strong pressure gradient that drives liquid towards the left; this lateral capillary pumping action quickly drives liquid out of the cavity. Thus, most of the filament stretching motion occurs when both contact lines are outside the cavity and the dynamics is roughly the same as that of a filament stretching between flat plates, as studied by Dodds *et al.* (2009). Despite the fact that the plate is under rotation relative to the cavity, the liquid fraction is $\phi = 0.5$. Three-dimensional calculations by Dodds *et al.* (2012) of filament stretching between plates with a rotating upper surface have shown that high angular velocities are necessary to break the symmetry of the liquid transfer.

To the best of our knowledge, this is the first time that such behaviour has been captured with numerical simulations. This was only possible because the present model considers the complete kinematics that fully describes the relative motion between the substrate and the cavity, which includes extension, shearing and rotation. This, in addition to the low capillary number, allows the development of a lateral capillary pumping that is strong enough to pull all the liquid out of the cavity. This lateral capillary pumping was observed experimentally by Yin & Kumar (2006) for different conditions and kinematics. In their experiments, a curved top surface slid horizontally over a cavity filled with liquid. In some conditions, the asymmetry between the front and rear menisci created a high enough curvature difference between the two sides of the cavity to give rise to the phenomenon already described in our results, with the difference that here the curvature gradient is created by the

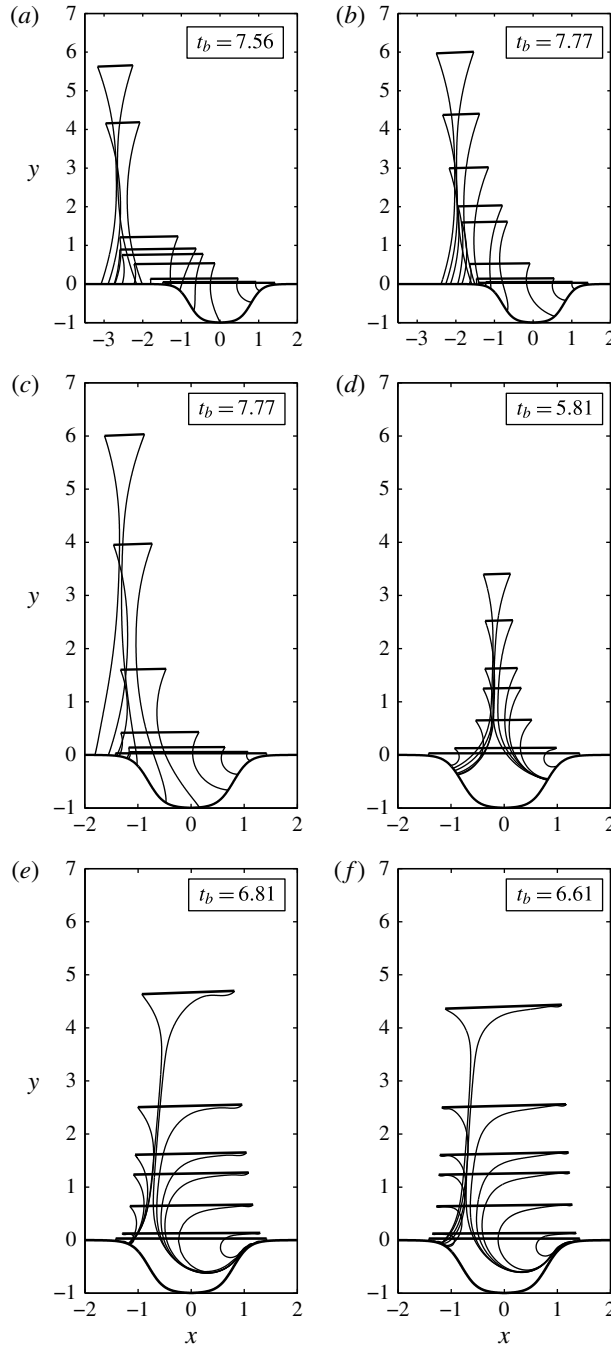


FIGURE 15. The free surface evolution accompanying the emptying of the cavity (groove) for (a) $Ca = 0.01$, (b) $Ca = 0.025$, (c) $Ca = 0.05$, (d) $Ca = 0.15$, (e) $Ca = 0.5$ and (f) $Ca = 1.0$.

imposed plate kinematics. Another piece of experimental evidence that shows that, in certain conditions, the filament breakup occurs with the contact lines outside the cavity is presented by Chuang *et al.* (2008). They show images of the surface of the

gravure roll after the liquid has been transferred to the substrate. In other cases, the remaining liquid drop is located outside the cavity, which is shown as completely empty. This is exactly what is predicted in our analysis.

As shown in figure 14, the liquid fraction increases slightly with the capillary number, reaching $\phi \simeq 0.6$ for $Ca = 0.025$. The evolution of the interface is shown in figure 15(b). The dynamics is very similar to the previous case, but with one important difference. Because the capillary forces are weaker (higher Ca), the pressure gradient that drives liquid out the cavity is smaller and this reduces the contact line velocities. As a result, when the filament begins to thin, the left contact line is outside the cavity, but the right contact line is still inside and becomes pinned at the corner of the groove during most of the filament extension. This asymmetry moves the breakup plane closer to the cavity, leading to a larger liquid volume being transferred to the top plate.

From $Ca = 0.025$ to $Ca = 0.15$, the liquid fraction ϕ decreases as the capillary number increases. Figure 15(c) shows the interface evolution for $Ca = 0.05$. The process is again similar to that when $Ca = 0.025$, but now the contact line speeds are lower because of the weaker capillary forces. When the liquid bridge begins to thin, the left contact line is near the corner of the groove and the right contact line is still near the bottom surface of the cavity. The restricted movement of the left contact line causes the pinch-off to occur closer to the top plate, leading to a smaller ϕ . The minimum value of ϕ occurs when $Ca = 0.15$, with the corresponding interface evolution shown in figure 15(d). For this case the capillary force is not strong enough to pump liquid out of the groove. Then, both contact lines remain inside the cavity during the entire process until breakup.

At even higher capillary number, e.g. $Ca = 0.5$ in figure 15(e), the contact lines at the top and bottom surfaces have very low mobility during the entire process. Thus, the wetted area on the top plate is considerably larger when compared with previous cases and, consequently, so is the volume of liquid attached to the top plate. As result, ϕ shows a local maximum. Finally, for $Ca = 1$ in figure 15(f), the contact lines are virtually immobile and their displacement is negligible during the entire process. Although this produces an even larger wetted surface on the upper plate, less liquid is removed from the cavity and the fraction ϕ presents a small decrease.

As mentioned before, reports of experiments on liquid transfer from single grooves are scarce. We have included data from Yin & Kumar (2006) and Chuang *et al.* (2008) for comparison purposes, even though their experiments do not correspond directly to the problem analysed in this section. Yin & Kumar (2006) used an upscaled trapezoidal cavity with an aspect ratio of $r_c = 1.2$. They studied the liquid transfer not to a rotating cylinder, but to a curved plate that slid over the top of the cavity. They found that the liquid fraction ϕ was virtually constant at $\phi = 0.5$ at low capillary numbers ($Ca < 5 \times 10^{-3}$) and decreased monotonically for $5 \times 10^{-3} < Ca < 5 \times 10^{-2}$. Figure 14 only presents the data in the range we have explored with our model. Chuang *et al.* (2008) worked with trapezoidal cells with an aspect ratio of $r_c = 0.83$ and used a rotating roll over the cavity to remove the liquid from the cell, i.e. the same kinematics as we have used in our analysis. They also used upscaled cavities, where inertial and gravitational effects may be important; moreover, the parameter $R_b \sim 170$ was much smaller than those used in our analysis. However, in agreement with the results of Yin & Kumar (2006), they found that ϕ decreases as the capillary number increases over the range explored. Despite the differences in the imposed kinematics and geometrical parameters, the predictions and the experimental data show the same general trend in the corresponding Ca range. It is important to note

that the predicted increase of ϕ for $10^{-2} < Ca < 2 \times 10^{-2}$ is small and it would be very difficult to capture experimentally. Unfortunately, we do not know of experiments on gravure printing for $Ca > 0.1$ and thus we cannot validate the predicted change of behaviour of ϕ as a function of Ca .

Kapur (2003) presented experimental results on gravure coating in the range $10^{-2} < Ca < 10^{-1}$. He used trapezoidal cavities of the order of 100 μm with different aspect ratios. His results indicate that ϕ increases almost linearly with Ca , showing a completely different trend from the experiments shown in figure 14. However, in gravure coating techniques, a continuous liquid film is deposited on the substrate; thus, the transferred liquid fraction must be calculated on average by comparing the final film thickness with the cavity volume per unit area of the substrate. In addition, because of the continuous film formed on the substrate, the liquid transfer process may be very different from the one that occurs in single cells, for which the dynamics of the contact lines has a strong effect on the volume of liquid transfer. Therefore, it is not clear how gravure coating results might be used as a basis for comparison with our predictions.

5. Final remarks

The fundamental aspects of gravure printing can be better understood by analysing the liquid transfer from a cell or groove to a rotating roll. In this work we have analysed two important aspects of this problem. First, we compared the liquid transfer dynamics from an axisymmetric cell, which is used to print dots, and a groove, which is used to print lines. In order to keep the flow 2-D for both cases, the comparison was made considering that the plate moves only vertically over the cell; the liquid bridge is simply stretched. This simpler kinematics is usually used as a simplified model to describe the complex relative motion between a substrate and a gravure cell. The results show that the azimuthal curvature of the interface, which occurs in the case of a cell, induces a lower mobility of the contact line and a stronger pinning at the corner of the cell. This contact line restriction reduces the amount of liquid that is transferred to the plate. Therefore, the predictions suggest that it is easier to remove liquid from grooves than from cells. This should be taken into consideration when designing gravure rolls to print a complex pattern of lines, as in the case of flexible circuits.

In order to verify the effect of the kinematics on the dynamics of the process, we have used a complete description of the relative motion between a substrate and a groove, by considering extension, shearing and rotation. The results show that the kinematics has a tremendous effect on the interface deformation and contact line displacements and, consequently, on the amount of liquid that is transferred to the substrate.

From an application point of view, the aforementioned results show that the amount of liquid transferred to the substrate depends strongly on the capillary number of the flow, which is a function of the liquid viscosity, substrate speed and roll radius. The relative lateral and rotational motions between the groove and roll surface lead to an interface that presents different curvatures on each side of the liquid filament. At low capillary number, the strong capillary pressure gradient and the mobile contact lines promote a lateral pumping that helps to remove liquid from the cavity. Approximately 50% of the liquid is transferred to the substrate and, because of the lateral pumping, all liquid is removed from the cavity. The liquid not transferred to the substrate remains on the lands between cavities. As an unwanted effect, the printed pattern

may be distorted and loss of registration may also occur because of the high contact line mobility. The lateral displacement of the printed pattern could be controlled by special substrate treatments to promote contact line pinning even at low capillary number, as suggested by Darhuber, Troian & Wagner (2001).

In contrast, printing at high capillary number has the advantages of a smaller contact line mobility, which produces less distortion in the transferred image and better registration. This conclusion agrees with the experimental observation of Darhuber *et al.* (2001), which shows that higher ink viscosity and extensional velocity between the surfaces avoid unwanted lateral ink redistribution during printing. The smaller transferred liquid fraction observed at high capillary number could be controlled by reducing the diameter of the rolls, which promotes better liquid removal from cavities.

The results show that the use of an accurate kinematic description between the cavity and the substrate is only necessary for low capillary numbers, for which the lateral displacement of the contact lines is important. For high capillary numbers, the transferred liquid fraction is mainly controlled by stretching and a simpler extensional motion is apparently sufficient to get reliable predictions. Since the liquid transfer is strongly affected by the contact line motion, a more accurate model of the flow near the contact lines should improve the accuracy of the predictions. It could include, for example, the dependence of the contact line velocity on the dynamic contact angle and hysteresis.

Acknowledgements

The authors would like to thank the following institutions for financial support: Consejo Nacional de Investigaciones Científicas y Técnicas of Argentina (CONICET), Fundação de Amparo à Pesquisa do Estado do Rio de Janeiro (FAPERJ) and the program 'Industrial Partnership for Research in Interfacial and Material Engineering' (IPRIME) of the University of Minnesota.

REFERENCES

- BENKREIRA, H. & PATEL, R. 1993 Direct gravure roll coating. *Chem. Engng Sci.* **48** (12), 2329–2335.
- BLAKE, T. D. 2006 The physics of moving wetting lines. *J. Colloid Interface Sci.* **299** (1), 1–13.
- CAIRNCROSS, R. A., SCHUNK, P. R., BAER, T. A., RAO, R. R. & SACKINGER, P. A. 2000 A finite element method for free surface flows of incompressible fluids in three dimensions. Part 1. Boundary fitted mesh motion. *Intl J. Numer. Meth. Fluids* **33**, 375–403.
- CAMPANA, D. M., UBAL, S., GIAVEDONI, M. D. & SAITA, F. A. 2007 Stability of the steady motion of a liquid plug in a capillary tube. *Ind. Engng Chem. Res.* **46**, 1803–1809.
- CHRISTODOULOU, K. N., KISTLER, S. F. & SCHUNK, P. R. 1997 *Advances in Computational Methods for Free-Surface Flows*. Chapman Hall.
- CHRISTODOULOU, K. N. & SCRIVEN, L. E. 1992 Discretization of free surface flows and other moving boundary problems. *J. Comput. Phys.* **99** (1), 39–55.
- CHUANG, H.-K., LEE, C.-C. & LIU, T.-J. 2008 An experimental study of the pick-up of scaled-up gravure cells. *Intl Polym. Process.* **23**, 216–222.
- CHUNG, D.-Y., HUANG, J., BRADLEY, D. C. & CAMPBELL, A. J. 2010 High performance, flexible polymer light-emitting diodes (PLEDs) with gravure contact printed hole injection and light emitting layers. *Org. Electron.* **11**, 1088–1095.
- COMSOL Multiphysics 1998–2013 Comsol. <http://www.comsol.com/>.
- DARHUBER, A. A., TROIAN, S. M. & WAGNER, S. 2001 Physical mechanisms governing pattern fidelity in microscale offset printing. *J. Appl. Phys.* **90** (7), 3602–3609.

- DING, J. M., VORNBROCK, A. F., TING, C. & SUBRAMANIAN, V. 2009 Patternable polymer bulk heterojunction photovoltaic cells on plastic by rotogravure printing. *Solar Energy Mater. Solar Cells* **93**, 459–464.
- DODDS, S. 2011 Stretching and slipping liquid bridges: liquid transfer in industrial printing. PhD thesis, University of Minnesota.
- DODDS, S., CARVALHO, M. S. & KUMAR, S. 2009 Stretching and slipping of liquid bridges near plates and cavities. *Phys. Fluids* **21**, 092103.
- DODDS, S., CARVALHO, M. S. & KUMAR, S. 2011 Stretching liquid bridges with moving contact lines: the role of inertia. *Phys. Fluids* **23**, 092101.
- DODDS, S., CARVALHO, M. S. & KUMAR, S. 2012 The dynamic of three-dimensional liquid bridges with pinned and moving contact lines. *J. Fluid Mech.* **707**, 521–540.
- GUPTA, C., MENSING, G. A., SHANNON, M. A. & KENIS, P. J. A. 2007 Double transfer printing of small volumes of liquids. *Langmuir* **23**, 2906–2914.
- HODA, N. & KUMAR, S. 2008 Boundary integral simulations of liquid emptying from a model gravure cell. *Phys. Fluids* **20**, 092106.
- HUANG, W.-X., LEE, S.-H., SUNG, H. J., LEE, T.-M. & KIM, D.-S. 2008 Simulation of liquid transfer between separating walls for modelling micro-gravure-offset printing. *Intl J. Heat Fluid Flow* **29**, 1436–1446.
- HUH, C. & SCRIVEN, L. E. 1971 Hydrodynamic model of steady movement of a solid/liquid/fluid contact line. *J. Colloid Interface Sci.* **35**, 85–101.
- KANG, H. W., SUNG, H. J., LEE, T.-M., KIM, D.-S. & KIM, C.-J. 2009 Liquid transfer between two separating plates for micro-gravure-offset printing. *J. Micromech. Microengng* **19**, 015025.
- KAPUR, N. 2003 A parametric study of direct gravure coating. *Chem. Engng Sci.* **58**, 2875–2882.
- KREBS, F. 2009 Fabrication and processing of polymer solar cells: a review of printing and coating techniques. *Solar Energy Mater. Solar Cells* **93**, 394–412.
- LAI, W. M., RUBIN, D. & KREMPL, E. 1999 *Introduction to Continuum Mechanics*. 3rd edn. Butterworth-Heinemann.
- LAMB, S. H. 1975 *Hydrodynamics*. 6th edn. Cambridge University Press, London, UK.
- LEE, T.-M., LEE, S.-H., NOH, J.-H., KIM, D.-S. & CHUN, S. 2010a The effect of shear force on ink transfer in gravure offset printing. *J. Micromech. Microengng* **20** (125026), 1–8.
- LEE, T.-M., NOH, J.-H., KIM, C. H., JO, J. & KIM, D.-S. 2010b Development of a gravure offset printing system for the printing electrodes of flat panel display. *Thin Solid Films* **518**, 3355–3359.
- POWELL, C. A., SAVAGE, M. D. & GUTHRIE, J. T. 2002 Computational simulation of the printing of Newtonian liquid from a trapezoidal cavity. *Intl J. Numer. Meth. Heat Fluid Flow* **12** (4), 338–355.
- PUDAS, M., HAGBERG, J. & LEPPÄVUORI, S. 2004a Gravure offset printing of polymer inks for conductors. *Prog. Org. Coat.* **49**, 324–335.
- PUDAS, M., HAGBERG, J. & LEPPÄVUORI, S. 2004b Printing parameters and ink components affecting ultra-fine-line gravure-offset printing for electronics applications. *J. Eur. Ceram. Soc.* **24**, 2943–2950.
- PULKRABEK, W. W. & MUNTER, J. D. 1983 Knurl roll design for stable rotogravure coating. *Chem. Engng Sci.* **38** (8), 1309–1314.
- SANTA-NOKKI, H., KALLIOINEN, J., KOLOLUOMA, T., TUBOLTSEV, V. & KORPPI-TOMMOLA, J. 2006 Dynamic preparation of TiO₂ films for fabrication of dye-sensitized solar cells. *J. Photoch. Photobio. A* **182**, 187–191.
- SCHENK, O. & GÄRTNER, K. 2004 Solving unsymmetric sparse systems of linear equations with PARDISO. *J. Future Gener. Comput. Syst.* **20** (3), 475–487.
- SHIKHMURZAEV, Y. D. 2006 Singularities at the moving contact line. Mathematical, physical and computational aspects. *Physica D* **217** (2), 121–133.
- SNOEIJER, J. H. & ANDREOTTI, B. 2013 Moving contact lines: scales, regimes, and dynamical transitions. *Annu. Rev. Fluid Mech.* **45**, 269–292.
- SPRITTLES, J. E. & SHIKHMURZAEV, Y. D. 2012 Finite element framework for describing dynamic wetting phenomena. *Intl J. Numer. Meth. Fluids* **68**, 1257–1298.

- UBAL, S., XU, B., DERBY, B. & GRASSIA, P. 2012 Continuous deposition of a liquid thread onto a moving substrate. Numerical analysis and comparison with experiments. *J. Fluids Engng* **134** (2), 021301.
- WEINSTEIN, S. J. & RUSCHAK, K. J. 2004 Coating flows. *Annu. Rev. Fluid Mech.* **36**, 29–53.
- YIN, X. & KUMAR, S. 2006 Flow visualization of the liquid-emptying process in scaled-up gravure grooves and cells. *Chem. Engng Sci.* **61**, 1146–1156.